Single-ended Fault Detection Scheme Using Support Vector Machine for Multi-terminal Direct Current Systems Based on Modular Multilevel Converter

Guangyang Zhou, Xiahui Zhang, Minxiao Han, Shaahin Filizadeh, and Zhi Geng

***Abstract*—This paper proposes a single-ended fault detection scheme for long transmission lines using support vector machine (SVM) for multi-terminal direct current systems based on modular multilevel converter (MMC-MTDC). The scheme overcomes existing detection difficulties in the protection of long transmission lines resulting from high grounding resistance and attenuation, and also avoids the sophisticated process of threshold value selection. The high-frequency components in the measured voltage extracted by a wavelet transform and the amplitude of the zero-mode set of the positive-sequence voltage are the inputs to a trained SVM. The output of the SVM determines the fault type. A model of a four-terminal DC power grid with overhead transmission lines is built in PSCAD/EMTDC. Simulation results of EMTDC confirm that the proposed scheme achieves 100% accuracy in detecting short-circuit faults with high resistance on long transmission lines. The proposed scheme eliminates mal-operation of DC circuit breakers when faced with power order changes or AC-side faults. Its robustness and time delay are also assessed and shown to have no perceptible effect on the speed and accuracy of the detection scheme, thus ensuring its reliability and stability.**

***Index Terms*—Fault detection, short-circuit fault, multi-terminal direct current systems based on modular multilevel converter, support vector machine (SVM), wavelet transform.**

I. INTRODUCTION

MULTI-TERMINAL direct current systems based on modular multilevel converter (MMC-MTDC) systems are a promising option for the future power grids. With their advantages of small harmonic contents and by enabling multiple power supply and infeed paths, MMC-MTDC systems offer economic benefits, the diversity in power generation and consumption, and consequentially a decrease in capacity investments. An MMC-MTDC system can improve the dynamic performance of the connected AC grid by providing emergency power supply in the event of large disturbances, which helps prevent blackouts and improve system stability [1], [2].

Currently, MMCs based on half-bridge submodules are the dominant topologies in MMC-MTDC systems. Despite their well-known benefits, these converters do not have fault clearing capability, as the fault current will not be cut off by blocking the converters and the AC grid will continue to feed the faulted DC circuit [3]. In addition, overcurrent concerns caused by faults in MMC-MTDC are aggravated by the presence of multiple converters combined with low system impedance. Therefore, fault detection in such systems must be completed in a short time period to enable timely and effective protection measures. For example, in the four-terminal Zhangbei grid in China, a detection time of 3 ms or less is required [4]. The faulted line must be correctly identified to minimize the impact of the fault on the overall system. The design of fault detection schemes that meet the specific requirements of MMC-MTDC systems is an urgent problem.

Existing literature shows two classes of widely adopted fault detection schemes, i. e., the schemes based on the boundary conditions provided by DC line reactors and based on travelling waves. The former class of schemes use thresholds of the voltage or current [5], [6], or the calculated power [7], which are proven to be effective. However, their dependability and selectivity depend on line reactors, and they face the difficulty in identifying faults with a high resistance. The latter class of schemes overcome these drawbacks. According to the measurement of the initial voltage traveling wave, [8]-[11] achieve short-circuit fault detection with high resistance utilizing single-ended measurements by comparing the multi-resolution morphological gradient, the arrival time, differential voltage, and the amplitudes, respectively. The inherent drawbacks of the latter class of schemes are their weak tolerance for measurement error of the wavehead of the initial travelling wave. Meanwhile, the aforemen-

Manuscript received: June 24, 2021; revised: October 2, 2021; accepted: December 2, 2021. Date of CrossCheck: December 2, 2021. Date of online publication: February 4, 2022.

This work was supported by the 111 project (No. B08013).

G. Zhou (corresponding author), X. Zhang, M. Han, and Z. Geng are with the School of Electrical and Electronic Engineering, North China Electric Power University, Beijing 102206, China (e-mail: sunshinezgy@126. com; zhangxiahui97@163.com; hanminxiao@263.net; gengz220@126.com).

S. Filizadeh is with the Department of Electrical and Computer Engineering, University of Manitoba, Winnipeg, Canada (e-mail: shaahin. filizadeh@umanitoba.ca).

DOI: 10.35833/MPCE.2021.000404

tioned fault detection schemes inevitably require the threshold value selection, which is indeed difficult in an MTDC system, since the system contains multiple converters and transmission lines. Circumventing this requires novel methods and techniques.

Artificial intelligence (AI) algorithms are powerful tools in solving non-linear problems and have been widely used in pattern recognition. Various AI algorithms including fuzzy systems [12], expert systems [13], rough set theory [14], Bayes classifier [15], neural networks (NNs) [16], and support vector machines (SVMs) [17] have already been applied in fault detection in power systems, among which NN-based algorithms are the most widely investigated. Artificial neural networks (ANNs) have shown to be effective for fault detection in AC power grids in [16], and their performance in high-voltage direct current (HVDC) system is also verified in [18] with the ability to enable both DC bus and DC line protection. In [19] , a comprehensive protection scheme containing 13 ANNs is proposed for a voltage source converter based HVDC (VSC-HVDC) system. However, their computation complexity and time delay are unacceptable for MTDC systems, so is the scheme proposed in [20] that relies on two ANNs with complex structures for fault detection. A one-dimensional convolutional neural network (CNN) is adopted in [21] for fault identification in a single MMC with four submodules. This method requires large amounts of data for offline training of CNN. Meanwhile, its reported detection time of 1.35 ms fails to meet the stringent requirements of complex DC power grids. Fault detection and location in MMC-MTDC systems are achieved based on recurrent neural network (RNN) in [22]. However, measurements including voltage, current, and power are adopted to ensure the accuracy of fault detection, not to mention the algorithmic complexity of RNN itself.

Compared with NN-based algorithm, SVM adopts the principle of structural risk minimization (SRM), which guarantees better performance and accuracy of generalization. Additionally, its advantages also lie in solving small-sample, nonlinear or high-dimensional pattern recognition problems, with the ability to overcome the problems of curse of dimensionality and over-fitting. Combined with discrete wavelet transform (DWT), an SVM-based fault classification scheme is applied in an AC power transmission system [23]. Applications of SVM in distribution systems and MMCs are presented in [24] and [25], respectively. However, no research work on the application of SVM for fault detection in MMC-MTDC systems is yet reported.

This paper proposes an SVM-based and communication-less fault detection scheme that features security, speed, selectivity, and sensitivity. Based on the analysis of the measured voltage after fault, its frequency spectrum is obtained using fast Fourier transform (FFT). The high-frequency component in the voltage can be used to identify internal and external faults. After symmetrical component analysis (SCA), two features, i. e., the second-level detailed coefficient further extracted by DWT and the zero-mode set of the positive-sequence voltage are obtained from the measured voltage. An integrated SVM-based fault detection scheme, which has the ability to recognize four different fault types, is presented, whose inputs are the two extracted features. Test results show the proposed scheme can achieve accurate fault detection for the whole length of the protected line, and has high sensitivity to the faults with high resistance. It achieves 100% internal fault detection without misjudgment of non-operating conditions. The proposed scheme is compared with other methods, and its robustness against measurement errors and time delay of the fault detection process are evaluated. It is concluded that the proposed scheme with only voltage measurement can provide fast and accurate fault detection in MMC-MTDC systems.

The rest of the papers are organized as follows. Section II shows the fault characteristics in MMC-MTDC systems. The design of SVM-based fault detection scheme is described in Section III. Section IV presents the performance evaluation. The robustness, merits, and applicability to larger systems of the proposed scheme are discussed in Section V. Section VI concludes the paper.

II. Fault Characteristics in MMC-MTDC Systems

A. System Structure

The four-terminal bipolar MMC-HVDC grid considered in this paper is shown in Fig. 1, where T1-T4 represent terminals 1-4, and F1-F3 represent the faults. All MMCs in the system have the same number of submodules per arm N_{sm} and the same submodule capacitance C_{sm}. L_{dc} is the smoothing reactor, which is installed at both ends of each transmission line with the same inductance. System parameters are listed in Table I.

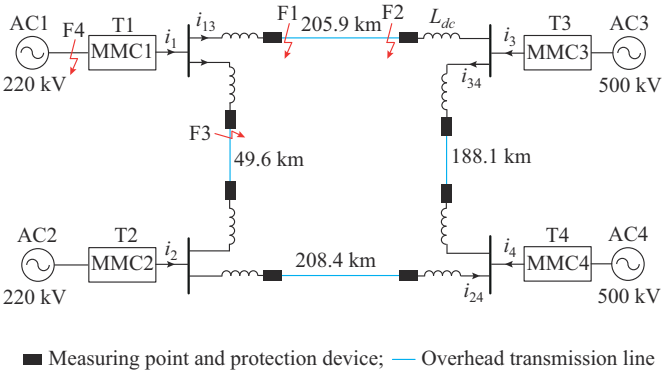

Fig. 1. Diagram of four-terminal bipolar MMC-HVDC grid.

TABLE I
Parameters of MMC-HVDC Grid

Description	Value
Rated DC voltage U_{dc}	±500 kV
L_{dc}	300 mH
Arm reactor of MMC L_{arm}	100 mH
N_{sm}	300
C_{sm}	12 mF
Power rating for MMC1, MMC3	1500 MW
Power rating for MMC2, MMC4	3000 MW

Long-distance overhead transmission lines are represented using frequency-dependent distributed-element based long-distance overhead transmission line models, as shown in Fig. 2, where r_0, l_0, g_0, and c_0 are the line resistance, inductance, conductance, and capacitance per unit of length, respectively; a1-a4 represent the nodes 1-4; G1 and G2 represent the ground wires; and C1 and C2 represent the conductors. The structure of the frequency-dependent overhead line model and the tower model in EMT simulations are shown in Fig. 2(b). The simulation setup in PSCAD of transmission line is listed in Table II.

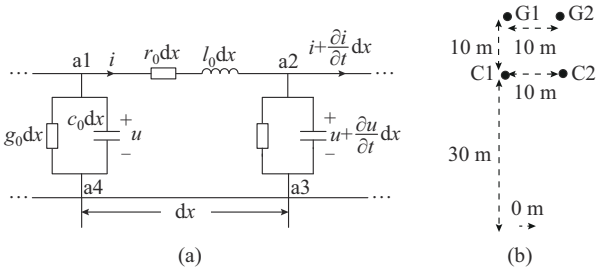

Fig. 2. Frequency-dependent distributed-element based long-distance overhead transmission line models. (a) Equivalent circuit of one transmission line unit. (b) Frequency-dependent overhead transmission line and tower model used in EMT simulations.

TABLE II
SIMULATION SETUP IN PSCAD OF TRANSMISSION LINE

Description	Simulation Setup
Conductor	Chukar
Ground wire	1/2 high strength steel
Ground resistivity	100 Ω·m

B. Fault Voltage Analysis

The inception of a short-circuit fault can be emulated by imposing an additional voltage source at the fault location that has an equal but opposite amplitude to the initial voltage. This inserted source will generate traveling waves that propagate to both ends of the transmission line. As shown in Fig. 3, V_0 is the inserted voltage source; R_f is the grounding resistance; and i_m and i_n are the currents of terminals m and n, respectively. The positive direction of the current is from bus to line, as marked in Fig. 3.

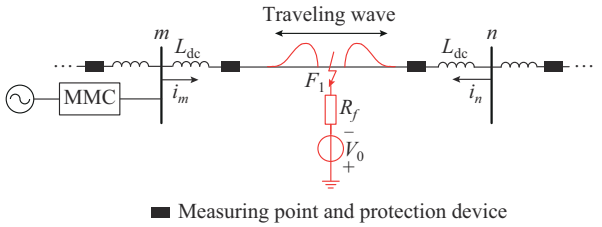

Fig. 3. Propagation of traveling waves after a fault.

According to the superposition theorem, the system with a short-circuit fault can be regarded as the addition of the load and the fault components. Taking terminal m as an example, the initially measured voltage and current after the fault are expressed as:

$$\begin{cases} u_m(t) = u_{ml} + u_{mf} \\ i_m(t) = i_{ml} + i_{mf} \end{cases} \tag{1}$$

where u_{ml} and i_{ml} are the load components; and u_{mf} and i_{mf} are the fault components.

The fault travelling wave consists of a series of harmonic-form frequencies, therefore, the measured voltage at the protection point contains high-frequency components [18], [26]. However, when the traveling wave propagates from the faulted point to the adjacent line, its high-frequency components will be suppressed by the smoothing reactor installed at the terminal of the line. At the same time, since the traveling wave will refract and reflect at the end of the transmission line, the amplitude of the traveling wave measured by the adjacent line is further reduced.

Taking the measurement at T1 side on line L13 is as an example, three short-circuit fault types, at T1 side on L13, at T3 side on L13, and at T1 side on L12 are tested, which are marked as F1, F2, and F3, respectively. The voltage waveform and frequency spectra under different fault conditions are shown in Fig. 4. It is clearly illustrated that, compared with the internal fault, the high-frequency part of the measured voltage in the case of an external fault attenuates significantly.

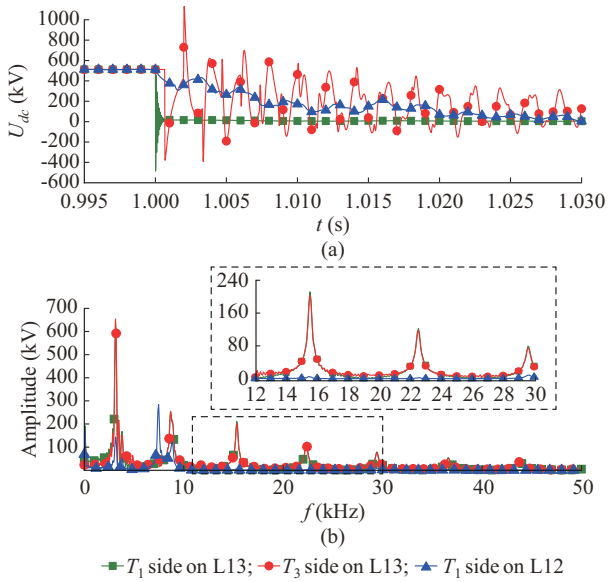

Fig. 4. Voltage waveform and frequency spectra under different fault conditions. (a) Voltage waveform. (b) Voltage frequency spectra.

C. SCA

For the DC transmission line, there is inter-coupling between the positive- and negative-pole components, which brings difficulty in fault analysis. The method of SCA analysis provides a decoupling approach [27].

Assuming A_p and A_n are positive- and negative-pole components, respectively, they can be decomposed as:

$$\begin{cases} A_p = A_{p1} + A_{p0} \\ A_n = A_{n1} + A_{n0} \end{cases} \tag{2}$$

where A_{p0} and A_{n0} are the zero-mode sets; and A_{p1} and A_{n1} are the line-mode sets. The relationship between zero- and line-mode sets is:

$$\begin{cases} A_{p1} = -A_{n1} \\ A_{p0} = A_{n0} \end{cases} \tag{3}$$

Keeping the electric power invariant in the transformation and combining (2) and (3), A_{p0} and A_{p1} can be obtained by:

$$\begin{bmatrix} A_{p0} \\ A_{p1} \end{bmatrix} = \frac{1}{2}\begin{bmatrix} 1 & 1 \\ 1 & -1 \end{bmatrix}\begin{bmatrix} A_p \\ A_n \end{bmatrix} \tag{4}$$

A negative-pole-to-ground fault is taken as an example and its schematic is illustrated in Fig. 5(a), where u_{fp} and i_{fp} are the voltage and current of the positive pole, respectively; u_{fn} and i_{fn} are the voltage and current of the negative pole, respectively; and R_g is the fault resistance.

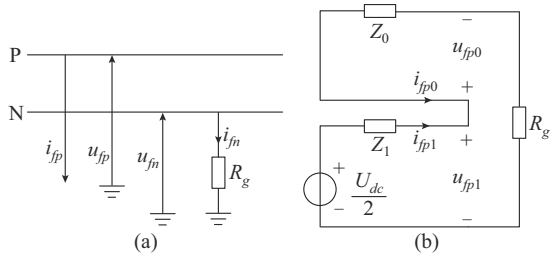

Fig. 5. Analysis of negative-pole-to-ground fault. (a) Negative-pole-to-ground fault. (b) Sequence-network for negative-pole-to-ground fault.

Before the inception of the fault, $u_{fp} = -u_{fn} = U_{dc}/2$ is satisfied. Thus, according to (4), the pre-fault conditions of zero-mode component u_{fp0} and the line-mode component u_{fp1} of the positive voltage may be written as:

$$\begin{cases} u_{fp1} = \dfrac{U_{dc}}{2} \\ u_{fp0} = 0 \end{cases} \tag{5}$$

Based on Fig. 5(a), the conditions after the fault are:

$$\begin{cases} i_{fp} = 0 \\ u_{fn} = i_{fn} R_g \end{cases} \tag{6}$$

Consequently, the following equations can be obtained considering the SCA as:

$$\begin{cases} i_{fp1} + i_{fp0} = 0 \\ -u_{fp1} + u_{fp0} = (i_{fp0} - i_{fp1}) R_g \end{cases} \tag{7}$$

The relationship between the line- and zero-mode sets of the positive voltage and current can be described as (8), which is depicted in Fig. 5(b).

$$\begin{cases} \dfrac{U_{dc}}{2} = i_{fp1} Z_1 + u_{fp1} \\ -i_{fp0} Z_0 = u_{fp0} \end{cases} \tag{8}$$

where Z_1 and Z_0 are the line- and zero-mode impedances, respectively, and can be obtained by:

$$\begin{cases} Z_0 = Z_s + Z_m \\ Z_1 = Z_s - Z_m \end{cases} \tag{9}$$

where Z_s and Z_m are the self-impedance and the mutual impedance of the transmission lines, respectively.

Substituting (8) in (7), the line- and zero-mode sets of the positive voltage can be obtained as:

$$\begin{cases} u_{fp0} = \dfrac{U_{dc} Z_0}{2(2R_g + Z_0 + Z_1)} \\ u_{fp1} = \dfrac{U_{dc}(Z_0 + 2R_g)}{2(2R_g + Z_0 + Z_1)} \end{cases} \tag{10}$$

It is noticeable that the amplitude of u_{fp1} is greater than u_{fp0} when the short-circuit fault occurs with high resistance. Besides, according to [8], the zero-mode set propagates low- and high-frequency parts of the signal attenuated much more severely compared with the line-mode component.

III. Design of SVM-based Fault Detection Scheme

A. Fault Area Identification

Based on the analysis in Section II, the high-frequency components in the line-mode set of the positive voltage u_{fp1} are suitable for the internal and external fault identifications. Here, DWT, which offers excellent time-frequency localization characteristics, is adopted to extract high-frequency components from signals.

Consider a given discretized measured signal $x[n]$. Its DWT is given as:

$$DWT(m,n) = \frac{1}{\sqrt{a_0^m}} \sum_k x(k) \psi\left(\frac{k - n b_0 a_0^m}{a_0^m}\right) \tag{11}$$

where $\psi(t)$ is the mother wavelet function. The scale and translation parameters, i.e., a and b in the continuous wavelet transform, are discretized as a_0^m and $nb_0a_0^m$, respectively. Here, $a_0 > 1$ and $b_0 \neq 1$ are the scale and translation steps, respectively; and m and n are the integers to guarantee the change of $\psi(t)$ in scale and translation, respectively.

As a typical DWT algorithm, multiresolution analysis (MRA) is able to decompose a signal into a set of frequency bands and is adopted in this paper. Figure 6 demonstrates a three-level decomposition of a signal according to MRA.

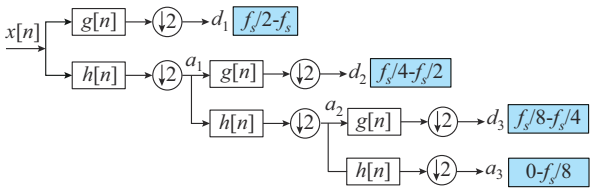

Fig. 6. Three-level decomposition of a signal according to MRA.

After passing through the high-pass filter $g[n]$ and low-pass filter $h[n]$, the original signal $x[n]$ that is sampled at a frequency of f_s is decomposed into a detail information d_1 and a coarse approximation a_1, which are associated with the high-frequency $(f_s/2 - f_s)$ and low-frequency $(0 - f_s/2)$ parts of the signal, respectively. a_1 is further passed through the same high-pass and low-pass filters, which generate the second-level DWT detail coefficient $d_2\,(f_s/4 - f_s/2)$, and approxi-

mate coefficient $a_2(0-f_s/4)$, respectively. Then, a_2 can be decomposed repeatedly in a similar manner. The generated detail and approximate coefficients at the j^{th} level are as follows:

$$\begin{cases} d_j[n]=\sum_k h[k-2n]a_{j-1}[k] \\ a_j[n]=\sum_k l[k-2n]a_{j-1}[k] \end{cases} \tag{12}$$

The modulus maximum values generated by the wavelet transform correspond to the mutation points of the original signal. To be specific, the magnitude indicates the strength of the signal mutation, and the polarity indicates the mutation direction [28]. In this paper, the Daubechies-3 (db3) wavelet is selected as the mother wavelet function, given that it is a compactly supported orthogonal wavelet basis with a small vanishing moment and low computation complexity [29].

In order to obtain enough data to ensure detection accuracy, the sampling frequency is set to be 100 kHz. Accordingly, the frequency bands after MRA corresponding to the first-, second-, and third-level reconstructed signals are 25-50 kHz, 12.5-25 kHz, and 6.25-12.5 kHz, respectively.

According to Fig. 6, the frequency range corresponding to the second-level detail coefficient d_2, has good potential to distinguish internal and external faults. Meanwhile, compared with d_1, it has better anti-noise interference capabilities. Hence, the summation of the second-level detail coefficient of u_{fp1}, as shown in (13), is selected as the index for the internal and external fault identifications.

$$D_{IE}=\sum_{n=n_0}^{n_0+N}\left|d_2(n)\right| \tag{13}$$

where n_0 is the sampling point when the protection device detects the inception of the fault; and N is the total number of samples. To guarantee protection speed, a window length of 0.5 ms is used in this paper, which yields $N=50$.

B. Fault Pole Discrimination

To discriminate the exact fault pole, i.e., positive-pole-to-ground (P-PTG), negative-pole-to-ground (N-PTG), or pole-to-pole (PTP), unique signatures from waveforms need to be extracted. Using the same method demonstrated in Section II-C, the zero-mode set of the positive voltage u_{fp0} under P-PTG and PTP fault can be written as:

$$u_{fp0}=\begin{cases} \dfrac{-Z_0U_{dc}}{2(2R_g+Z_0+Z_1)} & \text{P-PTG} \\ 0 & \text{PTP} \end{cases} \tag{14}$$

Based on observations from (10) and (14), the amplitudes of u_{fp0} under three different fault conditions, P-PTG, N-PTG, and PTP faults, are negative, positive, and zero, respectively. Simulation results in Fig. 7 verify the conclusion.

Therefore, these differences can be utilized to discriminate the faulty pole, and the summation of u_{fp0} is adopted to enlarge the disparity, as shown in (15).

$$D_{FT}=\sum_{n=n_0}^{n_0+N}u_{fp0} \tag{15}$$

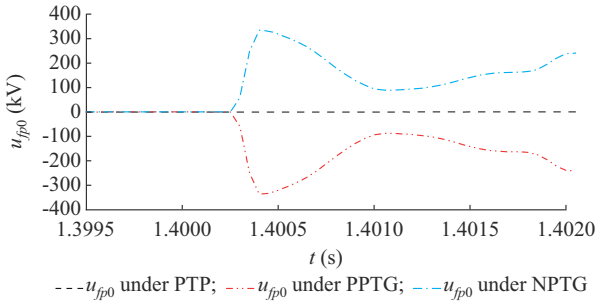

Fig. 7. Amplitudes of zero-mode set of positive voltage under three different fault conditions.

C. SVM Algorithm

The mechanism of SVM is to find an optimal classification hyperplane that meets the classification requirements of the training samples.

The goal of the hyperplane is to not only ensure correct classification, but also maximize the area at both sides of the hyperplane, as shown in Fig. 8, where the red cross and circle represent the support vectors.

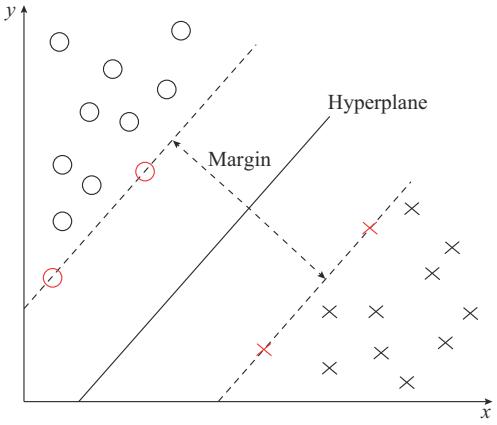

Fig. 8. Schematic diagram of SVM.

Given the training samples $(\boldsymbol{x}_i, y_i)$, $i=1, 2, \ldots n$, $\boldsymbol{x}\in\mathbf{R}^{\mathrm{d}}$, $y_i\in\{-1, 1\}$ and a hyperplane $\boldsymbol{H}$: $\boldsymbol{w}^{\mathrm{T}}\boldsymbol{x}+\boldsymbol{b}=\boldsymbol{0}$, where $\boldsymbol{w}\in\mathbf{R}^{\mathrm{d}}$ is a d-dimensional weight vector, and $\boldsymbol{b}\in\mathbf{R}$ is the bias term, the geometrical margin between the samples to the hyperplane can be written as:

$$r=\frac{\min y_i(\boldsymbol{w}^{\mathrm{T}}\boldsymbol{x}_i+\boldsymbol{b})}{\|\boldsymbol{w}\|} \tag{16}$$

To maximize the gap between the two sides of the hyperplane, the geometrical margin should be as great as possible. To simplify the analysis, set $\min y_i(\boldsymbol{w}^{\mathrm{T}}\boldsymbol{x}_i+\boldsymbol{b})=1$. Therefore, the aim becomes:

$$\max\frac{1}{\|\boldsymbol{w}\|} \tag{17}$$

It is equivalent to:

$$\min\frac{1}{2}\|\boldsymbol{w}\|^2 \tag{18}$$

If all the samples are separated correctly by the hyperplane, the following equation must be met by all samples:

$$y_i(\boldsymbol{w}^{\mathrm{T}}\boldsymbol{x}_i+\boldsymbol{b})\geq 1 \tag{19}$$

Taking the outliers caused by noise or measurement error into consideration, an optimal separating hyperplane can be found by solving the following quadratic programming problem:

$$\begin{cases}\min\left\{\dfrac{1}{2}\|\boldsymbol{w}\|^2+\dfrac{C}{2}\sum_{i=1}^{n}\xi_i^2\right\}\\ \text{s.t. } y_i(\boldsymbol{w}^{\mathrm{T}}\boldsymbol{x}_i+\boldsymbol{b})\geq 1-\xi_i \quad i=1,2,...,n\end{cases} \tag{20}$$

where C is the penalty term and is set to be 50; and ξ_i is the slack variable, which can be expressed as:

$$\xi_i=\max\{0,1-y_i(\boldsymbol{w}^{\mathrm{T}}\boldsymbol{x}_i+\boldsymbol{b})\} \tag{21}$$

Introducing the Lagrange function to solve this convex quadratic programming optimization problem yields:

$$\begin{cases}\min L(\alpha)=\dfrac{1}{2}y_iy_j\alpha_i\alpha_j\left(K(\boldsymbol{x}_i,\boldsymbol{x}_j)+\dfrac{\delta_{ij}}{C}\right)-\sum_{i=1}^{n}\alpha_i\\ \text{s.t. } \sum_{i=1}^{n}y_i\alpha_i=0 \qquad \alpha_i>0, i=1,2,...,n\end{cases} \tag{22}$$

where α_i is the Lagrange multiplier; $K(\cdot)$ is the kernel function (a linear kernel function is selected in this paper); and δ_{ij} is Kronecker's delta function in which $\delta_{ij}=1$ for $i=j$ and $\delta_{ij}=0$, otherwise.

Solving the dual problem in (22), the decision function for SVM can be obtained by:

$$f(x)=\mathrm{sgn}\left(\sum_{i=1}^{n}\alpha_i^*y_iK(\boldsymbol{x}_i,\boldsymbol{x}_j)+b^*\right) \tag{23}$$

where α_i^* and b^* are the parameters of the optimal classification hyperplane.

D. Start-up Criterion

To avoid erroneous and frequent protection activities during normal operation, a start-up criterion is designed. Since the DC line voltage will decrease dramatically after a fault, the trigger criterion utilizing an unusual voltage drop is proposed as:

$$\begin{cases}\left|u_{dcp}(t)\right|<U_{st}\\ \left|u_{dcn}(t)\right|<U_{st}\end{cases} \tag{24}$$

where u_{dcp} and u_{dcn} are the positive- and negative-pole voltages, respectively; and U_{st} is the start-up threshold value. According to [30], the most strict voltage limit for normal operation is 6%. In this paper, U_{st} is set to be 450 kV, i.e., 10% voltage drop considering some margin.

E. Overall Proposed Fault Detection Scheme

Based on the above analysis, the flowchart of the proposed scheme is shown in Fig. 9. Once the fault detection scheme is triggered by a low DC voltage, line- and zero-mode sets of the positive voltage u_{fp1} and u_{fp0} are extracted from the positive- and negative-pole voltage measurements on the same terminal through SCA. Two features D_{IE} and D_{FT} are then obtained from u_{fp1} after MRA and u_{fp0}, respectively. To acquire better classification results, these two features are normalized and then presented as inputs to the SVM. The normalization formula used is shown in (25):

$$x^*=\frac{x-x_{\min}}{x_{\max}-x_{\min}} \tag{25}$$

where $x_{\min}$ and $x_{\max}$ are the minimum and maximum values of the given data, respectively. Finally, the output of the SVM classifier gives the fault type.

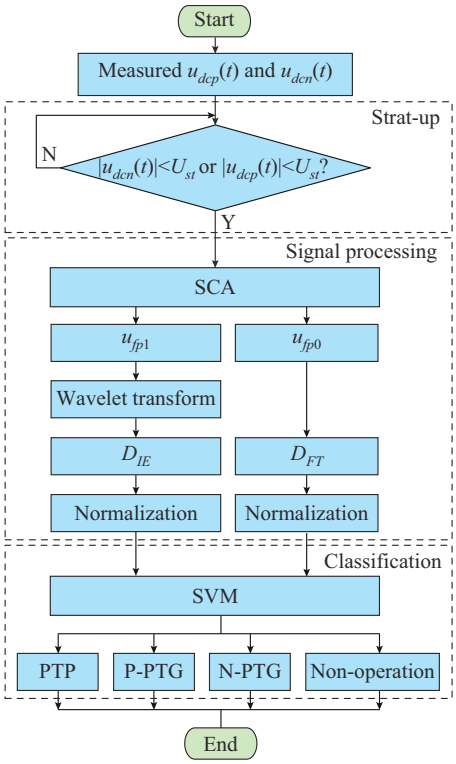

Fig. 9. Flowchart of proposed scheme.

IV. Performance Evaluation

In this section, the effectiveness of the proposed scheme is validated in the context of the four-terminal MMC-MTDC system shown in Fig. 1. The analysis is carried with the measurement equipment installed at T1 side on L13 as an example.

A. Fault Recognition Results

528 cases with various fault types, fault resistances, and fault locations are generated using PSCAD/EMTDC simulations, as listed in Table III.

TABLE III
Data Generated by PSCAD/EMTDC Simulations

Faulty line	Fault location	Fault resistance under PTP, P-PTG, N-PTG faults (Ω)	Number of samples
L13	Every 10 km on L13	0, 100, 200, 300, 400, 500, 600	420
L12	Every 10 km on L12	0, 100, 200	45
L34	Every 25 km on L34	0, 50, 100	63

Since the protection devices at T_1 side on L13 are used for analysis in this paper, short-circuit the faults occurring outside L13 are considered as external fault, whereas faults on L13 are considered internal under three fault conditions of P-PTG, N-PTG, and PTP, to be distinguished. Besides, external faults with a long distance from the L13 protection installation point or large grounding resistance will not cause a major, i.e., over 90%, voltage drop on L13, which implies that the protection algorithm on L13 will not be triggered.

The 528 samples are divided into a training set and a testing set for the SVM, as shown in Table IV. For the testing set, 30 samples are selected randomly from each of four different fault types. Hence, a testing set containing 120 samples is obtained.

TABLE IV
DATA FOR TRAINING AND TESTING

Type	Number of samples
Data for training	408
Data for testing	120

The appropriate SVM structure is obtained according to the training data, as shown in Fig. 10. Those support vectors used to distinguish different fault types are highlighted by pink circles and the black circles represent the data. The classification accuracy of the proposed scheme is verified with the testing data set, and its performance is evaluated in Fig. 11 and Fig. 12.

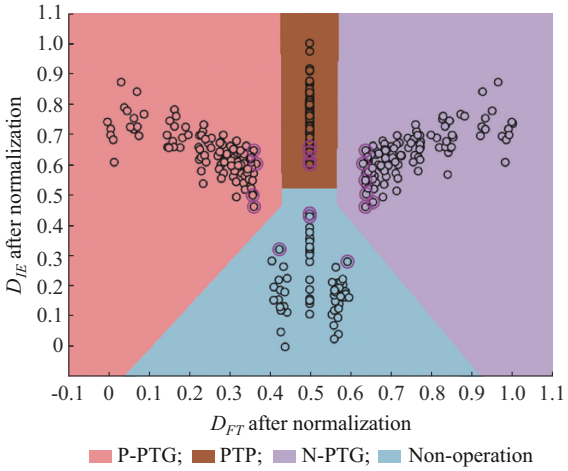

Fig. 10. Trained model of SVM with training data.

The proposed scheme can accurately distinguish different fault types. For the internal short-circuit fault, the proposed scheme can identify the fault inception swiftly for any position along the protected line. Therefore, the proposed scheme can realize fault detection of the whole transmission line, which is the core deficiency of the traveling wave-based scheme. Meanwhile, simulation results verify that the proposed scheme can identify short-circuit faults grounded with large resistance, i.e., 600 Ω (≈ 2 p.u.). This improves the fault detection that may occur on current changing based fault detection schemes with a short-circuit fault through large resistance. At the same time, even if a metallic short-circuit fault occurs at the beginning of an adjacent line, the proposed scheme can correctly recognize it as non-operation, thereby avoiding mal-operation of the protection devices.

Besides, as clearly indicated in the confusion matrix in Fig. 12, the accuracy of the proposed scheme is 100%, which proves its effectiveness to correctly identify and classify different fault types in an MTDC system.

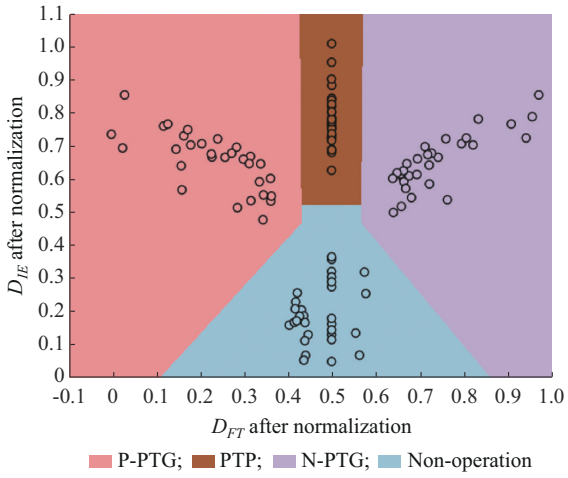

Fig. 11. Output of SVM with testing data.

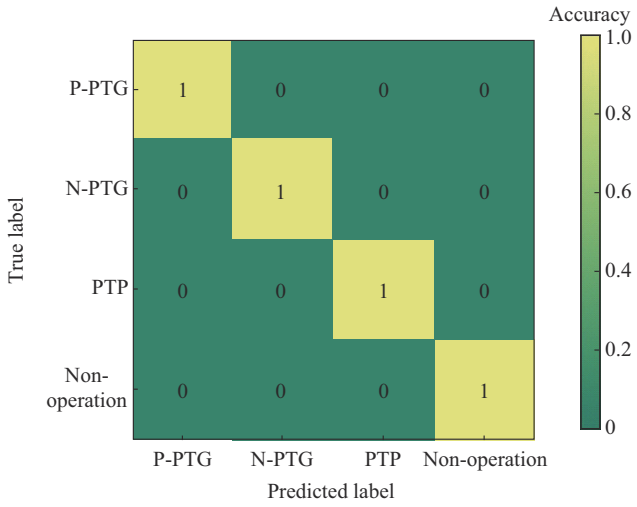

Fig. 12. Confusion matrix of classification effect.

B. Response to Power Order Change

In this subsection, the accuracy of the proposed scheme is assessed when the system undergoes a transient caused by a large power order change. As shown in Fig. 13, the power command of T_1 is reversed (from 1 p.u. to −1 p.u.) at $t = 1$ s, thus leading to a voltage drop on L13, which triggers the failure detection scheme. The measured single-ended voltage is then processed by the SCA and DWT, accordingly, obtaining d_2 and u_{fp0} shown above. Based on the proposed scheme, the calculated D_{IE} and D_{FT} are 5.8461 and 0.0086, respectively. After the normalization, the trained SVM correctly classifies this working condition as a non-operating category, as shown in Fig. 15, which verifies that the proposed scheme will not misjudge under routine power order change.

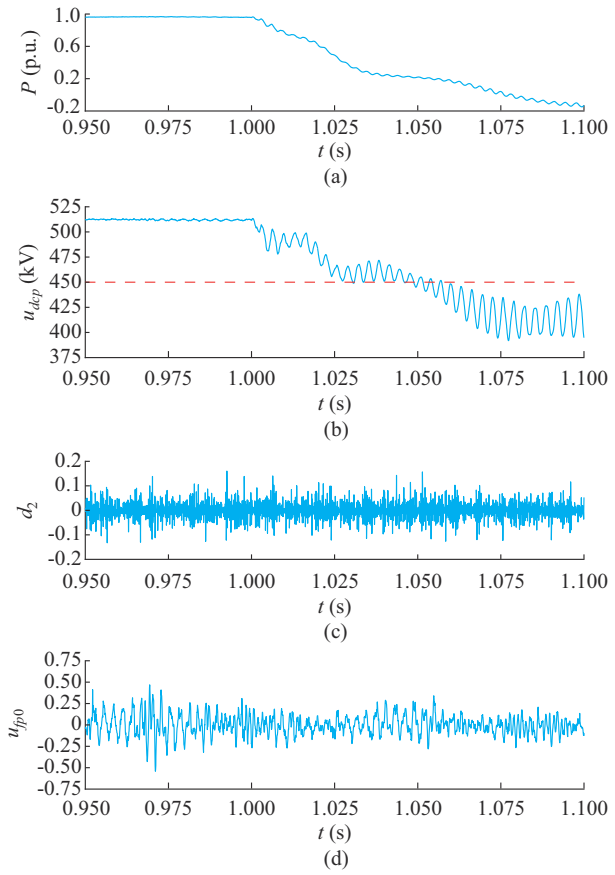

Fig. 13. Simulation results under power order change. (a) Power command of terminal 1. (b) Positive-pole voltage u_{dcp} on L13. (c) Second-level detailed coefficient. (d) Zero-mode set of positive-pole voltage.

C. Response to AC-side Fault

The accuracy of the classification output of the proposed scheme under an AC-side fault, i.e., F_4 in Fig. 1 when $t=1$ s, is discussed in this subsection, which will bring the most severe impact on the measured signal.

As illustrated in Fig. 14, subsequent to this short-circuit fault, the fault detection scheme is triggered for the measured DC voltage at the T1 side on L13 drops below the start-up threshold value. After obtaining d_2 and u_{fp0}, the calculated D_{IE} and D_{FT} are 1.0068 and −0.1646, respectively. The case classification result is shown in Fig. 15, which is correctly identified as non-operation category. Hence, no trip signal will be sent to DC circuit breakers on L13, avoiding any mal-operation.

Based on this observation, even when the most severe short-circuit fault occurs at the AC side and causes the most serious interference to the measured signal at the DC side, the proposed scheme can classify the fault type precisely.

D. Robustness Analysis

In practice, measurement errors will inevitably exist. In order to verify the effectiveness of the proposed scheme in such cases, the maximum voltmeter error of 0.5% [31] with a normal distribution is considered. This error is added to each measuring point and the classification result of the proposed scheme under noise is shown in Fig. 16.

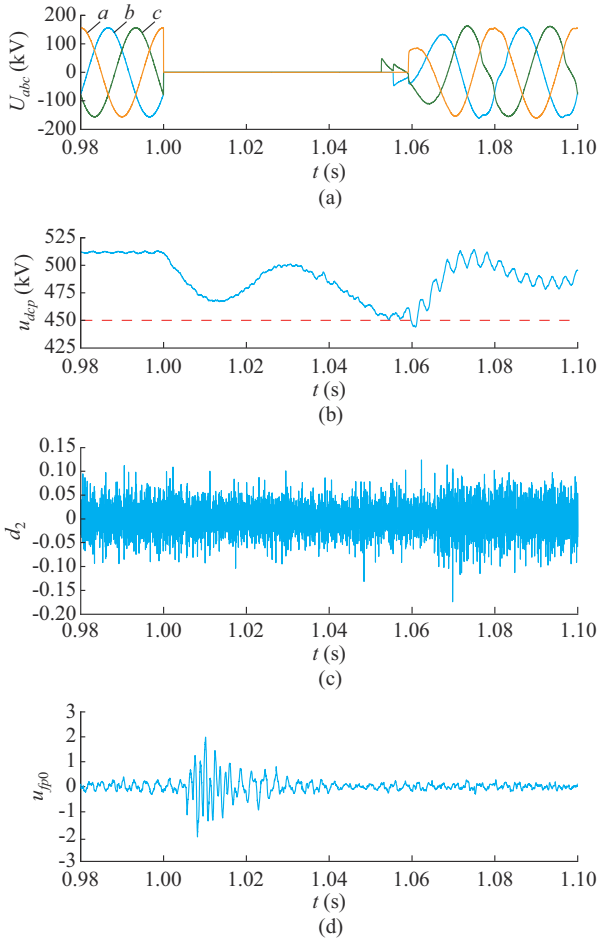

Fig. 14. Simulation results under AC-side fault. (a) AC-side three-phase voltage of T1. (b) Positive-pole voltage on L13. (c) Second-level detailed coefficient. (d) Zero-mode set of positive-pole voltage.

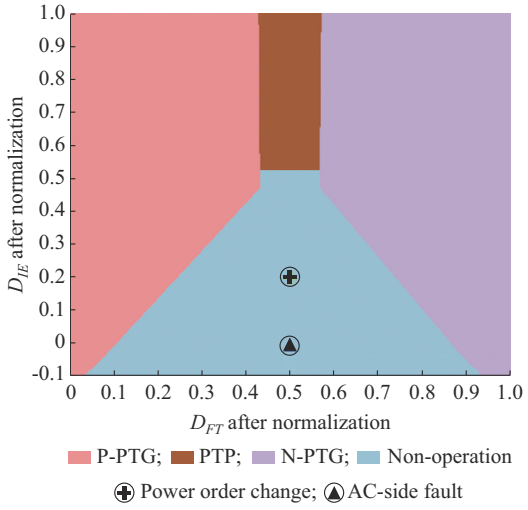

Fig. 15. Classification results of proposed scheme.

The accuracy of the classification result continues to be 100%. In other words, even if there are measurement errors, the proposed scheme can still accurately distinguish the four types of fault, which will avoid equipment malfunctions caused by the misjudgment of the detection scheme.

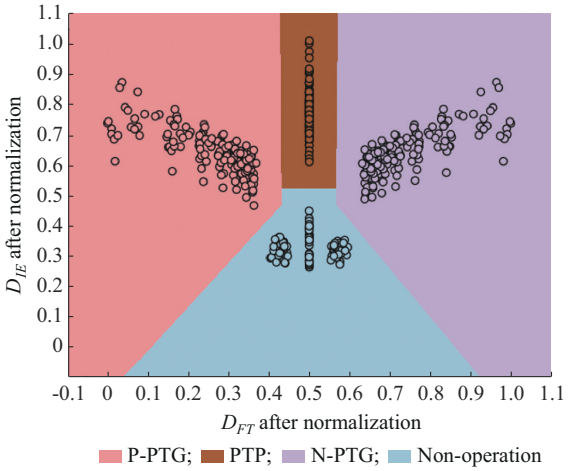

Fig. 16. Classification result of proposed scheme under noise.

V. Discussion

A. Time Delay Evaluation

Time delay is vital in assessing a fault detection scheme, given that the required fault detection time of a MTDC system is within 3 ms [4]. For the proposed scheme, the time delay is mainly composed of four parts: the fault wave propagation delay, sampling delay, computation delay in feature extraction, and the SVM classification delay.

For L13, the maximum propagation delay is about 0.68 ms, which only occurs when the short-circuit fault is incepted at T_3 side on L13, whereas the minimum propagation delay when the fault occurs at T_1 side on L13 is negligibly small. The sampling delay is set to be 0.5 ms, as mentioned in Section III-A to acquire enough data for the later fault detection. As for the computation delay, the proposed scheme is written in Python 3.8 and computed on the Intel Core i7 CPU with 8.0 GB of RAM. According to the test results, the computation delays for DWT and SCA are 1.12 ms and 0.241 ms, respectively. The classification time span for a single case in the trained SVM is presented as 0, for the running time of the algorithm is less than 1 μs. Based on the above analysis, the overall time delay of the proposed scheme is within 1.86 ms to 2.54 ms, which meets the requirement for a MTDC system, and the maximum value is demonstrated in Table V.

TABLE V
Time Delay for Proposed Scheme

Item	The maximum time span
Propagation delay	0.68 ms
Sampling delay	0.50 ms
Computation delay of DWT	1.12 ms
Computation delay of SCA	0.24 ms
Classification delay	< 1 μs
Overall time delay	2.54 ms

Hybrid DC circuit breakers are widely used in DC power grids. Once the short-circuit fault is detected by the proposed scheme, a trip signal is sent to the corresponding DC circuit breaker. The operation time of the hybrid DC circuit breaker, i. e., fault current transferred from the transfer branch to the energy absorption branch, is 3 ms, with the maximum breaking capacity of 15 kA [32]-[34]. Figure 17 illustrates the fault current waveforms under the most severe PTP short-circuit fault for different fault locations.

As shown above, when F_1 occurs, the current amplitude I_{13p} that the DC circuit breaker needs to cut off is 12.37 kA, whereas the current amplitude of F_2 is 6.36 kA. The two green dots on Fig. 17 further highlight the current amplitudes at the corresponding breaking time, taking the fault detection time and the operation time of DC circuit breaker into consideration. Under these two typical fault conditions, one has the shortest fault detection time with the fastest rate of rise of the fault current, and the other one has the longest fault detection time. Based on the simulation results, both the current amplitudes are within the breaking capacity of a hybrid DC circuit breaker without the assistance of additional current limiting devices. Therefore, the feasibility of the proposed scheme in practical application is confirmed.

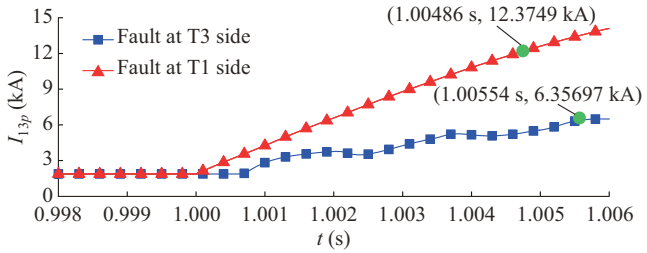

Fig. 17. Fault current waveform under the most severe PTP short-circuit fault for different fault locations.

B. Comparison with Existing Detection Schemes

In this subsection, the proposed scheme is compared with the existing detection scheme in terms of the maximum grounding resistance, the ability to achieve whole line protection, and whether a communication channel is required. Three typical fault detection schemes are selected, where [5], [8], and [18] represent the schemes based on the boundary conditions, traveling wave, and AI, respectively.

From Table VI, it can be observed that the proposed scheme has the greatest short-circuit fault with high resistance identification ability.

TABLE VI
Comparison with Other Schemes

Scheme	The maximum grounding resistance (Ω)	Whole line protection	The maximum detection time (ms)	Communication channel needed
Proposed scheme	600	Yes	2.540	No
[5]	0	Yes	0.700	Yes
[8]	300	No (90%)	2.616	Yes
[18]	350	Yes	2.180	No

Although the method in [5] is reported to have a smallest time delay in recognizing metallic short-circuit faults, the communication is inevitable in identifying the fault with re-

sistance, which undoubtedly will increase the detection time significantly. When a short-circuit fault occurs in the dead zone of the scheme in [8], backup protection is needed; otherwise, the DC circuit breaker on only one end will operate, since the other end will not perceive the fault inception. The ANN-based detection scheme in [24] performs better in fault detection. However, its fault identification accuracy for the faults with high resistance decreases to only 67.7%. This will cause mal-operation of the DC circuit breakers, and may adversely affect the security of the entire system. Based on the above analysis, the fault detection scheme proposed in this paper has clear advantages over the existing ones.

C. Applicability to Larger Systems

From the perspective of the effectiveness of the proposed scheme in a large system, only two inputs, D_{IE} and D_{FT}, are required for a trained SVM algorithm to determine a fault type in operation, as depicted in Fig. 9. This indicates that the input data is comprised of only two scalar quantities, no matter what the system scale is. In addition, the SVM algorithm is capable of handling tens or even hundreds of thousands of cases [35], [36]. For a specific protected DC system, the size of the data required to train a SVM is related to the number of lines connected to one DC bus, but not to the number of converters in the system, i.e., the system size. Besides, as demonstrated in Section IV-A, some external faults with a long distance from the protection installation point or large grounding resistance will not trigger the protection algorithm of the target line, which shrinks the number of the training cases.

From the perspective of the accuracy of the proposed scheme in a large DC system, the characteristics of the selected two inputs of the SVM algorithm are independent of system structure and scale. As is confirmed by the FFT results shown in Fig. 4, the summation of the second-level detail coefficient after multiresolution analysis of u_{fp1} and D_{IE} is calculated for the internal and external fault identifications. Also, the amplitudes of u_{fp0} have significant difference under three different fault conditions, which are negative, positive, and zero corresponding to P-PTG, N-PTG, and PTP faults, respectively. Thus, the summation of u_{fp0} and D_{FT} is adopted to discriminate the exact fault pole.

Based on the above discussion, there is no direct relationship between the grid scale and the number of cases required in SVM training. It also verifies the effectiveness and the accuracy in expanding the proposed scheme to more complex DC power grids.

VI. Conclusion

This paper proposes a single-ended fault detection scheme using SVM for MTDC systems based on MMC. According to the theoretical analysis of the high-frequency component in the line-mode set of the positive-pole voltage and the amplitude of the zero-mode set of the positive voltage, these two features are selected as the inputs and the SVM-based fault detection scheme is proposed. The test results indicate that, without complicated threshold value selection and relying merely on the single-ended voltage measurement, the proposed scheme can classify the four kinds of fault types, i. e., P-PTG, N-PTG, PTP, and the non-operation condition, with 100% accuracy even under faults with grounding resistances as high as 600 Ω. Besides, the possibility of mal-operation of DC circuit breakers when subjected to power order changes or AC-side three-phase faults can be avoided, and its robustness under the measurement error is verified. The time delay of the proposed scheme is proven to meet the requirements for DC grid protection, and the proposed scheme has the advantage of high fault identification accuracy for the whole protected line, which are crucial for the safe, fast, and stable operation of MTDC system. The limitation of the proposed scheme is that its sensitivity and selectivity can only be guaranteed for the considered system and based on large training data. This implies that the system needs to be trained for the specific system in which it is employed. It is worth noting that the requirement for retraining is a common feature and shortcoming of virtually all fault detection scheme based on AI algorithms.

References

[1] N. Ahmed, L. Ängquist, S. Mahmood *et al*., "Efficient modeling of an MMC-based multiterminal DC system employing hybrid HVDC breakers," *IEEE Transactions on Power Delivery*, vol. 30, no. 4, pp. 1792-1801, Aug. 2015.

[2] S. L. Blond, R. Bertho, D. V. Coury *et al*., "Design of protection schemes for multi-terminal HVDC systems," *Renewable and Sustainable Energy Reviews*, vol. 56, pp. 965-974, Apr. 2016.

[3] A. Raza, A. Akhtar, M. Jamil *et al*., "A protection scheme for multi-terminal VSC-HVDC transmission systems," *IEEE Access*, vol. 6, pp. 3159-3166, Mar. 2018.

[4] W. Xiang, S. Yang, L. Xu *et al*., "A transient voltage-based DC fault line protection scheme for MMC-based DC grid embedding DC breakers," *IEEE Transactions on Power Delivery*, vol. 34, no. 1, pp. 334-345, Feb. 2019.

[5] C. Li, A. M. Gole, and C. Zhao, "A fast DC fault detection method using DC reactor voltages in HVDC grids," *IEEE Transactions on Power Delivery*, vol. 33, no. 5, pp. 2254-2264, Oct. 2018.

[6] Y. Li, J. Li, L. Xiong *et al*., "DC fault detection in meshed MTDC systems based on transient average value of current," *IEEE Transactions on Industrial Electronics*, vol. 67, no. 3, pp. 1932-1943, Mar. 2020.

[7] S. Li, W. Chen, X. Yin *et al*., "A novel integrated protection for VSC-HVDC Transmission line based on current limiting reactor power," *IEEE Transactions on Power Delivery*, vol. 35, no. 1, pp. 226-233, Feb. 2020.

[8] N. Tong, X. Lin, X. Zhang *et al*., "The principle of in-situ ranging grounding protection for overhead multi-terminal flexible and direct power grids that do not rely on boundary elements," *Proceedings of the CSEE*, vol. 39, no. 7, pp. 2049-2060, Apr. 2019.

[9] X. Yu and L. Xiao, "A DC fault protection scheme for MMC-HVDC grids using new directional criterion," *IEEE Transactions on Power Delivery*, vol. 36, no. 1, pp. 441-451, Feb. 2020.

[10] B. Li, M. Lv, B. Li *et al*., "Research on an improved protection principle based on differential voltage traveling wave for VSC-HVDC transmission lines," *IEEE Transactions on Power Delivery*, vol. 35, no. 5, pp. 2319-2328, Oct. 2020.

[11] B. Li, Y. Li, J. He *et al*., "An improved transient traveling-wave based direction criterion for multi-terminal HVDC grid," *IEEE Transactions on Power Delivery*, vol. 35, no. 5, pp. 2517-2529, Oct. 2020.

[12] Z. Yi and A. H. Etemadi, "Fault detection for photovoltaic systems based on multi-resolution signal decomposition and fuzzy inference systems," *IEEE Transactions on Smart Grid*, vol. 8, no. 3, pp. 1274-1283, May 2017.

[13] J. C. Tan, P. A. Crossley, D. Kirschen *et al*., "An expert system for the back-up protection of a transmission network," *IEEE Transactions on Power Delivery*, vol. 15, no. 2, pp. 508-514, Apr. 2000.

[14] R. Ghimire, C. Zhang, and K. R. Pattipati, "A rough set-theory-based fault-diagnosis method for an electric power-steering system," *IEEE/ASME Transactions on Mechatronics*, vol. 23, no. 5, pp. 2042-2053,

Oct. 2018.
[15] Y. Xiang and J. F. G. Cobben, "A Bayesian approach for fault location in medium voltage grids with underground cables," *IEEE Power and Energy Technology Systems Journal*, vol. 2, no. 4, pp. 116-124, Dec. 2015.
[16] A. Abdullah, "Ultrafast transmission line fault detection using a DWT-Based ANN," *IEEE Transactions on Industry Applications*, vol. 54, no. 2, pp. 1182-1193, Apr. 2018.
[17] W. Li, X. Miao, and X. Zeng, "Short circuit fault type identification of low voltage AC system based on black hole particle swarm and multi-level SVM," in *Proceedings of 2020 Chinese Automation Congress (CAC)*, Shanghai, China, Nov. 2020, pp. 1-6.
[18] W. Xiang, S. Yang, and J. Wen, "ANN-based robust DC fault protection algorithm for MMC high-voltage direct current grids," *IET Renewable Power Generation*, vol. 14, no. 2, pp. 199-210, Feb. 2020.
[19] V. L. Merlin, R. C. D. Santos, S. L. Blond *et al*., "Efficient and robust ANN-based method for an improved protection of VSC-HVDC systems," *IET Renewable Power Generation*, vol. 12, no. 13, pp. 1555-1562, Oct. 2018.
[20] Q. Yang, S. L. Blond, R. Aggarwal *et al*., "New ANN method for multi-terminal HVDC protection relaying," *Electric Power Systems Research*, vol. 148, pp. 192-201, Jul. 2017.
[21] S. Kiranyaz, A. Gastli, L. Ben-Brahim *et al*., "Real-time fault detection and identification for MMC using 1-D convolutional neural networks," *IEEE Transactions on Industrial Electronics*, vol. 66, no. 11, pp. 8760-8771, Nov. 2019.
[22] Q. Yang, J. Li, R. Santos *et al*., "Intelligent fault detection and location scheme for modular multi-level converter multi-terminal high-voltage direct current," *High Voltage*, vol. 6, no. 1, pp. 125-137, Feb. 2021.
[23] A. A. Zakri, S. Darmawan, J. Usman *et al*., "Extract fault signal via DWT and penetration of SVM for fault classification at power system transmission," in *Proceedings of 2018 2nd International Conference on Electrical Engineering and Informatics (ICon EEI)*, Batam, Indonesia, Oct. 2018, pp. 191-196.
[24] X. G. Magagula, Y. Hamam, J. A. Jordaan *et al*., "Fault detection and classification method using DWT and SVM in a power distribution network," in *Proceedings of 2017 IEEE PES PowerAfrica*, Accra, Ghana, Jun. 2017, pp. 1-6.
[25] Y. Yang, L. Ke, and Y. Liu, "Fault detection method of modular multilevel converter based on current mean value and SVM," in *Proceedings of 2020 Chinese Control And Decision Conference (CCDC)*, Hefei, China, May 2020, pp. 4058-4063.
[26] Z. He and K. Liao, "Natural frequency-based protection scheme for voltage source converter-based high-voltage direct current transmission lines," *IET Generation, Transmission & Distribution*, vol. 9, no. 13, pp. 1519-1525, Oct. 2015.
[27] Y. Zhang, N. Tai, and B. Xu, "Fault analysis and traveling-wave protection scheme for bipolar HVDC lines," *IEEE Transactions on Power Delivery*, vol. 27, no. 3, pp. 1583-1591, Jul. 2012.
[28] S. Mallat and W. L. Hwang, "Singularity detection and processing with wavelets," *IEEE Transactions on Information Theory*, vol. 38, no. 2, pp. 617-643, Mar. 1992.
[29] I. Daubechies, "The wavelet transform, time-frequency localization and signal analysis," *IEEE Transactions on Information Theory*, vol. 36, no. 5, pp. 961-1005, Sept. 1990.
[30] J. Cao, W. Du, H. Wang *et al*., "Minimization of transmission loss in meshed AC/DC grids with VSC-MTDC networks," *IEEE Transactions on Power Systems*, vol. 28, no. 3, pp. 3047-3055, Aug. 2013.
[31] Texas Instruments. (2015, Feb.). AN-202 a digital multimeter using the ADD3501. [Online]. Available: https://www.ti.com/lit/an/snoa592c/snoa592c.pdf?ts=1642490035067&ref_url=https%253A%252F%252Fwww.ti.com%252Fsitesearch%252Fcn%252Fdocs%252Funiversalsearch.tsp% 253FlangPref% 253Den-US% 2526searchTerm% 253DAN-202%2526nr%253D11
[32] P. Verrax, A. Bertinato, M. Kieffer *et al*., "Transient-based fault identification algorithm using parametric models for meshed HVDC grids," *Electric Power Systems Research*, vol. 185, p. 106387, Aug. 2020.
[33] G. Zhou, M. Han, S. Filizadeh *et al*., "Studies on the combination of RSFCLs and DCCBs in MMC-MTDC system protection," *International Journal of Electrical Power & Energy Systems*, vol. 125, p. 106532, Feb. 2020.
[34] F. Mohammadi, K. Rouzbehi, M. Hajian *et al*., "HVDC circuit breakers: a comprehensive review," *IEEE Transactions on Power Electronics*, vol. 36, no. 12, pp. 13726-13739, Dec. 2021.
[35] T. Omrani, A. Dallali, B. C. Rhaimi *et al*., "Fusion of ANN and SVM classifiers for network attack detection," in *Proceedings of 2017 18th International Conference on Sciences and Techniques of Automatic Control and Computer Engineering (STA)*, Monastir, Tunisia, Dec. 2017, pp. 374-377.
[36] M. Fauvel, J. A. Benediktsson, J. Chanussot *et al*., "Spectral and spatial classification of hyperspectral data using SVMs and morphological profiles," *IEEE Transactions on Geoscience and Remote Sensing*, vol. 46, no. 11, pp. 3804-3814, Nov. 2008.

Guangyang Zhou received the B.Sc. degree in power system and its automation from North China Electric Power University, Beijing, China, in 2017, where she is currently pursuing her Ph.D. degree in electrical engineering. Her research interests include modular multilevel converter, high-voltage direct current and fault detection and protection in DC grids.

Xiahui Zhang received the B.S. degree from the China University of Geosciences, Beijing, China, in 2019. He is pursuing the M.D. degree with North China Electric Power University, Beijing, China. His research interests include DC distribution network and its control.

Minxiao Han received the Ph.D. degree in electrical engineering and automation from North China Electric Power University, Beijing, China, in 1995. He was a Visiting Ph.D. Student with Queen's University of Belfast, Belfast, U.K., and a Postdoctoral Fellow with Kobe University, Kobe, Japan. He is currently the Director of Institute of Flexible Electric Power Technology in North China Electric Power University. He has been the Leader in projects consigned by National Nature Science Foundation of China, National Educational Ministry, and enterprises. His research interests include applications of power electronics in power system including high-voltage direct current, flexible AC transmission systems, and power conversion and control.

Shaahin Filizadeh received the B.Sc. and M.Sc. degrees in electrical engineering the from Sharif University of Technology, Tehran, Iran, in 1996 and 1998, respectively, and the Ph.D. degree from the University of Manitoba, Winnipeg, Canada, in 2004. He is currently a Professor with the Department of Electrical and Computer Engineering, University of Manitoba. He is a Registered Professional Engineer in the Province of Manitoba. He is active in several IEEE committees and is currently the Chair of the IEEE Task Force on Dynamic Phasor Modeling Techniques. His research interests include electromagnetic transient simulation and power electronics.

Zhi Geng received the B.Sc. degree in electrical engineering from Jiangsu Normal University, Nanjing, China, in 2013, the M.Sc. degree in electrical engineering from Southeast University, Nanjing, China, in 2018. He is currently working toward the Ph.D degree with the School of Electrical and Electronic Engineering, North China Electric Power University, Beijing, China. His current research interests include modular multilevel converter, fault diagnosis, and DC grid.